

Large Horizontal Near-field Scanner based on a Non-tethered Unmanned Aerial Vehicle

*Original*

Large Horizontal Near-field Scanner based on a Non-tethered Unmanned Aerial Vehicle / Ciorba, Lorenzo; Virone, Giuseppe; Paonessa, Fabio; Righero, Marco; De Lera Acedo, Eloy; Matteoli, Stefania; Colin Beltran, Edgar; Bolli, Pietro; Giordanengo, Giorgio; Vecchi, Giuseppe; Magro, Alessio; Chiello, Riccardo; Peverini, Oscar A.; Addamo, Giuseppe. - In: IEEE OPEN JOURNAL OF ANTENNAS AND PROPAGATION. - ISSN 2637-6431. - ELETTRONICO. - 3:(2022), pp. 568-582. [10.1109/ojap.2022.3173741]

*Availability:*

This version is available at: 11583/2966625 since: 2022-06-10T12:01:06Z

*Publisher:*

IEEE-INST ELECTRICAL ELECTRONICS ENGINEERS INC

*Published*

DOI:10.1109/ojap.2022.3173741

*Terms of use:*

This article is made available under terms and conditions as specified in the corresponding bibliographic description in the repository

*Publisher copyright*

IEEE postprint/Author's Accepted Manuscript

©2022 IEEE. Personal use of this material is permitted. Permission from IEEE must be obtained for all other uses, in any current or future media, including reprinting/republishing this material for advertising or promotional purposes, creating new collecting works, for resale or lists, or reuse of any copyrighted component of this work in other works.

(Article begins on next page)

# Large Horizontal Near-field Scanner based on a Non-tethered Unmanned Aerial Vehicle

LORENZO CIORBA<sup>1</sup>, GIUSEPPE VIRONE<sup>1</sup>, FABIO PAONESSA<sup>1</sup>, MARCO RIGHERO<sup>2</sup>, ELOY DE LERA ACEDO<sup>3</sup>, STEFANIA MATTEOLI<sup>1</sup>, EDGAR COLIN BELTRAN<sup>4</sup>, PIETRO BOLLI<sup>5</sup>, GIORGIO GIORDANENGO<sup>2</sup>, GIUSEPPE VECCHI<sup>6</sup>, ALESSIO MAGRO<sup>7</sup>, RICCARDO CHIELLO<sup>8</sup>, OSCAR A. PEVERINI<sup>1</sup>, GIUSEPPE ADDAMO<sup>1</sup>.

<sup>1</sup>Institute of Electronics, Computer and Telecommunication Engineering, Italian National Research Council, 10129 Turin, Italy

<sup>2</sup>Advanced Computing, Photonics and Electromagnetics, LINKS Foundation, 10138 Turin, Italy

<sup>3</sup>Cavendish Laboratory, University of Cambridge, Cambridge, United Kingdom

<sup>4</sup>Conacyt, Instituto Nacional de Astrofísica, Óptica y Electrónica, Tonantzintla, Puebla, Mexico

<sup>5</sup>Astrophysical Observatory of Florence, INAF, 50125 Florence, Italy

<sup>6</sup>Department of Electronics and Telecommunication, Politecnico di Torino, 10129 Turin, Italy

<sup>7</sup>Institute of Space Sciences and Astronomy, University of Malta, Msida MSD 2080, Malta

<sup>8</sup>Department of Physics, University of Oxford, Oxford, United Kingdom

CORRESPONDING AUTHOR: Lorenzo Ciorba (e-mail: [lorenzo.ciorba@ieiit.cnr.it](mailto:lorenzo.ciorba@ieiit.cnr.it)).

**ABSTRACT** A horizontal planar scanner with an approximate size of  $40\text{ m} \times 40\text{ m}$  has been implemented using the Unmanned Aerial Vehicle (UAV) technology. The UAV is not wired to the ground to maintain the flexibility and short setup time of a non-tethered flight. In this configuration, the UAV-mounted continuous-wave source is not phase-locked to the on-the-ground receiver. A dual-polarized reference antenna placed on the ground is hence used to retrieve the relevant phase information. The presented approach has been applied on the Pre - Aperture Array Verification System (Pre -AAVS1) of the Square Kilometre Array, which is a digital beamformed array with 16 active elements. An inverse source technique has been applied on measured Near-Field (NF) data acquired on two different sets of points (one for each electric field component) from all the receiver channels. In this way, Embedded Element Patterns (EEPs), array calibration coefficients and pattern have been determined from NF data only. The achieved results have been validated using a complementary set of Far-Field (FF) measurements and simulations.

**INDEX TERMS** Antenna measurements, near-field measurements, unmanned aerial vehicle, digital beamforming array, phased-array radio telescopes, array calibration.

## I. INTRODUCTION

IN recent years, UAV technology has been experimented as antenna measurement solution [1] - [3] for very large antennas that cannot be placed in an anechoic chamber or have to be characterized in-situ. Due to its portability, low cost, and ability to perform arbitrary paths, the UAV proved to be a powerful tool for Far-Field (FF) measurements [4] - [13]. However, Near-Field (NF) strategies [14], [15] become necessary when the Antenna Under Test (AUT) is so large that the Fraunhofer distance (greater than hundreds of meters) is no longer compliant with flight altitude regulations. In these cases, a Near Field to Far Field (NF-FF) transformation can be used to determine the FF quantities of interest from NF data. Such technique generally requires the knowledge of both magnitude and phase of the sampled NF signal. However, in a UAV-based measurement setup, where source and receiver are generally not connected, the measured phase is continuously drifting during the flight.

One solution to overcome this problem is to connect (tether) the UAV to the ground equipment with a RF-over-fiber link [16], [15] to provide a valid phase reference. However, the UAV flight is constrained by the presence of the cable that



**FIGURE 1.** The UAV equipped with the transmitter, balun and dipole antenna flies over the array under test (pre AAVS1 array). On the right (inside the white circle): reference antenna exploited for the phase retrieval.

makes the flight more difficult to perform and to setup. This is especially cumbersome for horizontal scans where the UAV has to fly above the AUT. Another possibility is to resort to phaseless techniques [2], [17] or phase retrieval algorithms [18], [19], e.g., alternating minimization methods, least squares formulations and lifting methods. These methods rely on magnitude-only measurements and minimize a nonlinear and non-convex cost functional. For this reason, these

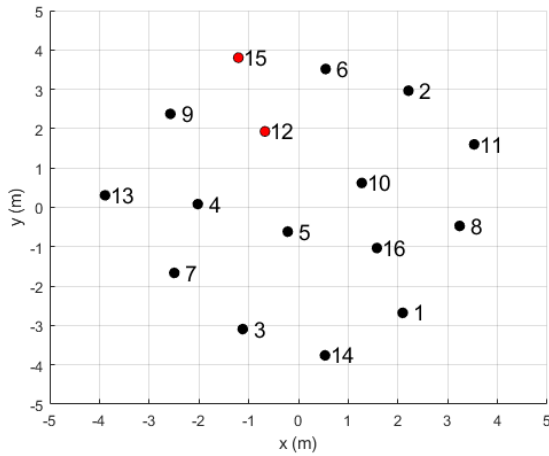


**FIGURE 2.** Configuration of the Pre - Aperture Array Verification System (Pre -AAVS1) and element numbers. Inner (element 12) and outer (element 15) elements are highlighted in red.

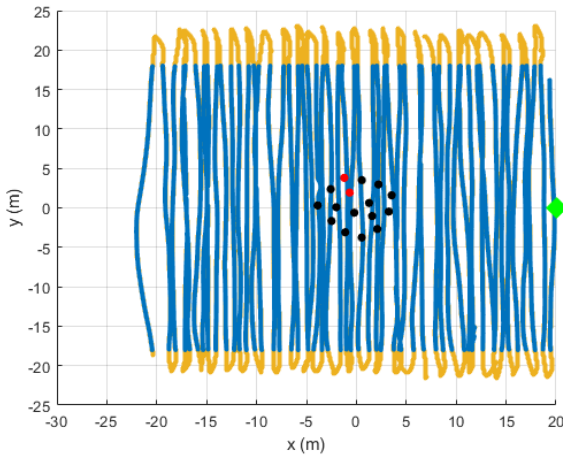


**FIGURE 3.** Yellow and blue line represent the UAV path for the y-oriented raster (view from above). Black, red and green dots represent the array, the considered elements and reference antenna, respectively.

techniques could lead to an ill-posed problem that suffers of local minima. Another possible solution to avoid phase measurements is the use of an additional (reference) link between source and receiver. This is the case of interferometric [20]-[21] and holographic techniques [22], [23] where magnitude-only measurements of combinations of direct and reference signal are generally used.

In this work, the additional link between source and receiver is achieved through a known antenna (herein after referred to as the *reference antenna*) that is placed in the proximity of the AUT (see Fig. 1). Signals from both the AUT and reference antenna are sampled (magnitude and phase) by a common receiver that is not phase-locked to the continuous-wave source placed on-board the UAV. A phase reconstruction method is hence proposed that uses the measured phase

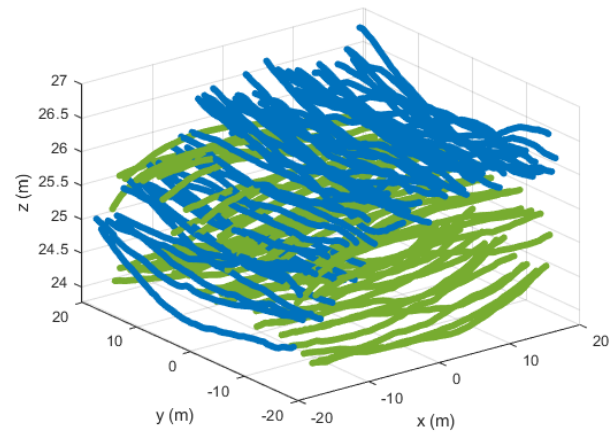


**FIGURE 4.** The extracted path for the two UAV flights: x-oriented (green) and y-oriented (blue line) rasters.

difference between AUT and the reference antenna signals. This method can be seen as a generalization of the standard procedure [24] found in FF test ranges which uses a reference antenna to retrieve the phase information. However, in the standard procedure, source and reference antenna are fixed while the AUT rotates. In the present UAV-based measurement setup, the source is instead moving with respect to both the AUT and the reference antenna (see Fig. 1). The proposed technique allows to maintain the advantages of a non-tethered flight. Furthermore, the NF-FF transformation problem remains linear through the availability of the reconstructed phase information.

Due to the non-regularity of the UAV path, (e.g., not planar, or spherical) the inverse source approach has been selected [25], [26] as NF-FF transformation strategy. This procedure allows to compute the desired FF pattern through equivalent electric and magnetic currents defined on a virtual surface enclosing the AUT. Such equivalent currents are determined from the NF measured data through an inverse problem.

Experimental results on a VHF array of 16 active elements with digital beamforming are used to demonstrate the technique. The considered array is the Pre - Aperture Array Verification System (Pre -AAVS1) (see Fig. 1) of the Square Kilometre Array [27]-[30] located at the Mullard Observatory in Cambridge (UK). Embedded Element Patterns (EEPs), calibration coefficients and array pattern are obtained from a horizontal NF planar scan with an approximate size of  $40\text{ m} \times 40\text{ m}$ . To the best of authors' knowledge, such a large size has never been reached with conventional mechanical scanners.

In Section II, the AUT and its digital acquisition system are presented. The measurement setup and the phase reconstruction method through the reference antenna are discussed in Section III. Results on the NF-FF transformation at 175 MHz are presented in Section IV. Finally, some conclusions are drawn.

The novel contributions of this work are:

- 1) A large (almost 40 m size) NF horizontal scanner that provides both magnitude and phase is implemented using a UAV;
- 2) Differently from other solutions in the literature, such a scanner is implemented using a non-tethered UAV to maintain flight flexibility, agility and short setup time;
- 3) The two tangential components of the electric field used as input in the NF-FF transformation are sampled on two different sets of points.
- 4) To the authors' knowledge, this is the first time that an inverse source NF-FF transformation is applied to UAV measurements of an array with digital beamforming.
- 5) The calibration of the digital beamformed array is performed on the transformed EEPs.

## II. The Antenna Under Test and Acquisition System

The results presented in this paper have been obtained during the development of the Square Kilometre Array (SKA) low-frequency instrument (50-350 MHz) [31]. In this framework, the Pre - Aperture Array Verification System (Pre -AAVS1) (see Fig. 1) is located in Mullard Observatory in Cambridge (UK) and is composed of 16 active dual-pol log-periodic elements arranged in a pseudorandom (aperiodic) configuration (see Fig. 2). The average inter-element (center-to-center) spacing is approximately 1.8 m. Each array element, called SKALA-2, is a 9-dipole log-periodic antenna equipped with a differential Low Noise Amplifier (LNA) integrated on the top. The antenna has a footprint of 1.2 m  $\times$  1.2 m and an overall height of 1.8 m. Detailed pictures, dimensions and performance can be found in [32], [33].

The array has an overall size of 9.2 m (see Fig. 2) and is placed over a ground plane mesh of 16-m diameter. One polarization is along South-North (y-axis) direction whereas the orthogonal polarization (x-axis) is in the West-East direction.

In this receiving system, the two polarizations of each antenna are connected to the analog inputs of a Tile Processing Module 1.2 (TPM) [34], the precursor to the TPM that is used for Phase One of the SKA. The TPM houses 32 Analog to Digital Converters (ADCs), with a programmable amplifier connected to each, and two Field Programmable Gate Arrays (FPGAs). The voltage signals are sampled at 800 MS/s, generating an observable band of 400 MHz. The digitized and amplified signals pass through a polyphase filter bank which splits the band into 512 frequency channels of  $\sim$ 92.6 kHz width, spaced by 781.25 kHz. Even if a real-time digital beamformer is present in this system, the beamforming has been performed offline exploiting all the digitized signals to achieve more flexibility e.g., perform offline calibration. A server hosts the monitoring and control software which can initialise and configure the TPMs [35], as well as the data acquisition system [36].

The large size of this radio telescope prototype oriented the development of the large NF scanner presented in this work. Moreover, the presence of active antennas constrained the UAV to operate in TX mode.

A previous prototype has been already characterized using a FF flights [30] with good results. The NF approach presented

in this work has been investigated as a valuable alternative for the test of even larger arrays, e.g., SKA-low full stations. For such arrays, the FF condition cannot be reached within the flight altitude regulation limits, generally of 120 meters.

## III. Near-Field Planar Scanner

Planar NF scanning is a well-established technique for antenna characterization [37]. The probe usually scans a rectangular grid with constant spacing (usually half wavelength) on a plane. Other planar acquisitions are also possible, e.g., spiral [38] or planar with non-constant spacing [39]. The measurement is usually combined with a NF-FF transformation in order to obtain the AUT pattern.

### A. UAV and scan strategy

The core of the proposed strategy is an Unmanned Aerial Vehicle (UAV) (Fig. 1) equipped with a continuous-wave RF source. Through a preprogrammed flight path, the UAV is capable to perform autonomous navigation. Quasi-planar flights (Fig. 3 - 4) were performed by the UAV acting as a NF scanner. More precisely, the micro hexacopter was equipped with a continuous-wave synthesizer, a balun and a dipole antenna. The transmitter power was 5 dBm. An attenuator of 30 dB was inserted in order not to saturate the antenna LNA. The UAV-mounted dipole (aluminum tube) was half wavelength at 175 MHz with a diameter of 6 mm. The UAV position was acquired by a differential GNSS system with a few centimeters of accuracy. Such position accuracy can be considered acceptable at the considered frequency of 175 MHz (wavelength 1.7 m). The UAV orientation was measured by the onboard Inertial Measurement Unit with an accuracy of about 2 degrees.

The dipole antenna onboard the UAV transmits only one field component. Therefore, two quasi-planar flights were performed to acquire both field components (labeled by x-oriented raster and y-oriented raster). In this scan strategy (differently from standard NF setups), the samples for the two field components are not co-located. Nevertheless, such information is manageable within the inverse source method described in Section IV-B.

The UAV path of the y-oriented raster is shown in Fig. 3 as a 2D view whereas both x-oriented and y-oriented rasters are shown together in Fig. 4 in a 3D fashion. Each of these two quasi-planar rasters scans a square area of approximately 40 m  $\times$  40 m. From each flight, a scan of 36 m  $\times$  36 m has been extracted as input for the NF-FF transformation. This is because measurement points where the UAV curved (yellow points in Fig. 3) are source of uncertainty due to the rapidly changing UAV angles (UAV angles are not properly sampled in these regions). For this reason, these points were discarded and rectilinear paths only (e.g., blue points in Fig. 3) were considered as input of the NF-FF transformation. During each flight, complex voltages were acquired at each array element by a complete digital back-end (already described in Section II). With a maximum speed of 3 m/s, the UAV flight time was about 15 minutes (without landing and takeoff) for each flight. The mean altitude of the UAV

flight was approximately 25 meters. Hence, the NF region of the array under test was scanned.

Flights were programmed as constant altitude rasters with a constant spacing of half wavelength (0.9 meters) between the parallel linear cuts. However, since the UAV is not capable to precisely follow the programmed flight (see the measured trajectories in Fig. 3 - 4), the half wavelength sampling criterion was not fulfilled in all the scanning regions (orthogonally to the UAV path direction, e.g., along x-axis for y-oriented raster, see Fig. 3), nevertheless, an average distance of half wavelength was achieved. The maximum (orthogonal) distance was about one wavelength, this condition occurs for less than one percent of the useful flight path (blue line in Fig. 3). On the other hand, the field is heavily oversampled along the UAV path thanks to the very fast receiving acquisition system on the ground (average distance between two successive samples is less than 1 cm). During each flight, the dipole over the UAV was always tangential to the UAV path e.g., in the x-oriented raster the dipole was almost aligned with the x-axis whereas in the y-oriented raster with the y-axis. In standard planar NF scans, the two tangential components of the electric field are acquired. Note that these two components are usually measured over the same spatial points. On the contrary, in the present measurement setup, the two components were acquired over two different sets of points (see Fig. 4). It is evident that such points follow surfaces that are not planar and not regular either. The altitude of the UAV trajectory ranges from 24 to 27 m, i.e., approximately two wavelengths at the considered frequency. In such a distance, the phase of the field can vary significantly (more than 360 degrees). Interpolations of data on a regular planar grid will hence require significant redundancy of measurement points (e.g., a cloud of points) which will in turn lead to prohibitive flight time. For this reason, standard NF-FF transformations are hardly applicable. All the results presented in this paper have been obtained with the inverse source technique (see Section IV-B). Such a technique is capable to efficiently deal with a set of measurement points with arbitrary locations.

### B. Near-Field Phase Reconstruction using Reference Antenna

Phase information is crucial to maintain the inverse source NF-FF transform linear and well-posed. In this work, a reference antenna (see Fig. 1, 3) is used to reconstruct the desired phase information. A preliminary attempt has already been performed in [40] with a single polarized reference antenna. The dual polarization capability of the reference antenna has been exploited in order to reconstruct the phase for both NF electric field components. As described in the following, this introduces an additional step to equalize phases from the two polarizations of the reference antenna.

The distance between the reference antenna and the AUT has to be sufficiently large in order not to perturb their field distribution. According to Fig. 3 (green diamond), the reference antenna is 20 m far from the array center, i.e.,

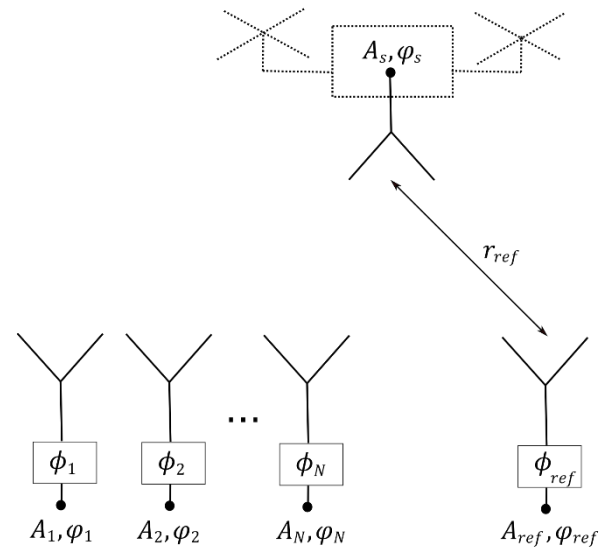


**FIGURE 5. Measurement setup. The UAV flies over the array and the reference antenna. Each antenna is dual polarized, only one output signal is shown for simplicity (superscripts (p) and (q) described in the text are understood).**

about 12 wavelengths. The combination of such distance and the UAV flight height justifies a FF interaction between source and reference antenna. Fig. 5 shows a scheme of the measurement setup where  $A_n^{(p)}, \varphi_n^{(p)}$  are the magnitude and phase of the received signal measured at the  $n$ -th element with polarization  $p$  (with the acquisition system described in Section II) for  $n = 1, \dots, N$  and  $p = x, y$  whereas  $A_s, \varphi_s$  are the magnitude and phase of the source signal ( $\varphi_s$  is unknown) onboard the UAV.

The phase difference needed to apply the NF-FF transformation to the  $n$ -th element can be expressed as

$$\Delta\varphi_{ns}^{(p)} = \varphi_n^{(p)} - \varphi_s \quad (1)$$

where the dependence on the relative position between source and AUT is understood. However,  $\varphi_s$  is unknown because the transmitter is not phase-locked to the receiver. Therefore, the phase variation between measurement points suffers from a drift (i.e., variation of  $\varphi_s$ ) between the UAV-mounted source frequency reference and the receiver clock.

In our approach  $\varphi_s$  is eliminated exploiting the measured phase  $\varphi_{ref}^{(q)}$  at the  $q$ -polarized reference antenna ( $q = x, y$ ), the knowledge of the reference antenna and source radiation pattern and their relative position and orientation. According to a FF approximation of the transmission link between the source and the reference antenna (determined from [41]), it can be shown that

$$\varphi_{ref}^{(q)} = \varphi_s - k_0 r_{ref} + [(\mathbf{p}_{ref}^{(q)} \cdot \mathbf{p}_s) + \phi_{ref}^{(q)}] \quad (2)$$

where  $k_0$  is the free-space wavenumber,  $r_{ref}$  is the distance between reference antenna and source,  $[\cdot]$  denotes the phase of a complex number,  $\mathbf{p}_s$  and  $\mathbf{p}_{ref}^{(q)}$  are the polarization unit vectors ( $\mathbf{p} = \mathbf{e}/|\mathbf{e}|$  where  $\mathbf{e}$  is the FF radiation pattern,  $\mathbf{E}(r, \theta, \phi) = \mathbf{e}(\theta, \phi) e^{-jk_0 r}/(4\pi r)$  is the electric field and

$(r, \theta, \phi)$  are the spherical coordinates; the dependance of the source position and orientation is understood) of the source and the reference antenna with polarization  $q$ , respectively, with  $q = x, y$ . It should be noted that  $\mathbf{p}_s$  and  $\mathbf{p}_{ref}^{(q)}$  contain the radiation pattern of UAV-mounted source and reference antenna, respectively. In this work, the source radiation pattern has been computed considering both the geometry of the dipole and the UAV frame using CST Microwave Studio. The reference antenna pattern has been simulated using FEKO (same model as AUT described in Section IV-A).

The phase shift  $\phi_{ref}^{(q)}$ , which is unknown, is related to all the components from the reference antenna to the digitizer including LNA, cables, the receiver. It is therefore independent of the relative position between the UAV and reference antenna. Similarly, (see Fig. 5) signals from all the array elements have unknown phase shifts  $\phi_n^{(p)}$ . It means that the reconstructed phase patterns will be computed up to addition by a constant phase shift. Their effect will be removed by the calibration procedure discussed in Section IV-C.

The unknown source phase  $\varphi_s$  can be computed from (2) and substituted into (1). In this way, the desired phase difference  $\Delta\varphi_{ns}^{(p)}$  is obtained

$$\Delta\varphi_{ns}^{(p)} = \varphi_n^{(p)} - \varphi_{ref}^{(q)} - k_0 r_{ref} + [(\mathbf{p}_{ref}^{(q)} \cdot \mathbf{p}_s) + \phi_{ref}^{(q)}] \quad (3)$$

Apart from the unknown phase constant  $\phi_{ref}^{(q)}$ , the right-hand side of (3) is fully determined by measured quantities ( $\varphi_n^{(p)}$ ,  $\varphi_{ref}^{(q)}$ ,  $r_{ref}$ , relative position and orientation) and a-priori knowledge of the source and reference antenna radiation patterns. It should be remembered that (3) implies the usage of a reference antenna located in the FF of the UAV-mounted source.

It should be noted that (3) does not contain  $\varphi_s$ . Therefore, the effect of its variation in time has been also eliminated. Such cancelation occurs in the difference  $\varphi_n^{(p)} - \varphi_{ref}^{(q)}$  because these two quantities are affected by the same drift between UAV-mounted source frequency reference and the receiver clock (see measurement scheme in Fig. 5). The phases  $\varphi_n^{(p)}$  and  $\varphi_{ref}^{(q)}$  are acquired coherently from two channels of the same digitizer.

The proposed technique can be seen as a generalization of the measurement solution traditionally adopted in standard FF test ranges which use a fixed reference antenna for phase measurements [24]. In the latter case, the source does not move with respect to the reference antenna (while the AUT rotates), therefore, the only varying term in the right-hand side of (3) is the phase difference  $\varphi_n^{(p)} - \varphi_{ref}^{(q)}$ . In this work, the terms  $k_0 r_{ref}$ ,  $[(\mathbf{p}_{ref}^{(q)} \cdot \mathbf{p}_s)]$  are instead exploited to account for the relative movement of the source with respect to the reference antenna.

In this work, y-polarized elements of Pre-AAVS1 (see Section II) are analyzed, i.e.,  $p = y$ . Equation (3) can be used when only one component of the electric field is measured (as in [40]), say the y component. In this case,  $q = p = y$  is chosen in (3). Then, NF-FF transformations

exploiting only one component of the field are applicable. For this purpose, only one flight (e.g., a y-oriented raster) is needed and the constant phase shift  $\phi_{ref}^{(q)}$  does not affect the reconstruction and its presence in (3) can be neglected. However, as it will be shown in Section IV-D (Fig. 22), the usage of only one NF component leads to inaccurate cross-polarization values.

When both components of the electric field are needed, samples along two orthogonal flights must be acquired (e.g., an x-oriented and a y-oriented raster). In this case, when the source polarization is orthogonal (or quasi-orthogonal) to the chosen reference antenna polarization, the signal received at the reference antenna may have a low signal-to-noise ratio. This degradation of the received signal may result in a poor phase reconstruction. For this reason, a dual-polarized reference antenna should be used, and the signal received through the polarization that matches the one of the source should be exploited. More precisely, for the data acquired along the x-oriented raster (3) is applied with  $q = x$  whereas for the data acquired along the y-oriented raster (3) is applied with  $q = y$ . In this way, polarization-matching between source and reference antenna is obtained and high signal-to-noise ratio for the measured receiving signal is ensured.

Since  $\phi_{ref}^{(x)}$  is generally different from  $\phi_{ref}^{(y)}$ , such a procedure leads to an unknown constant phase shift  $\phi_{ref}^{(y)} - \phi_{ref}^{(x)}$  between the two phase reconstructions from the two orthogonal flights. Due to this phase shift, the whole phase reconstruction is not coherent and cannot be directly used as input for a NF-FF transformation.

The unknown phase shift  $\phi_{ref}^{(y)} - \phi_{ref}^{(x)}$  can be evaluated performing the difference between equations (2) with  $q = x$  and (2) with  $q = y$ , i.e., eliminating again the common term  $\varphi_s$

$$\phi_{ref}^{(y)} - \phi_{ref}^{(x)} = \varphi_{ref}^{(y)} - \varphi_{ref}^{(x)} - [(\mathbf{p}_{ref}^{(y)} \cdot \mathbf{p}_s) + \phi_{ref}^{(x)}] + [(\mathbf{p}_{ref}^{(x)} \cdot \mathbf{p}_s) + \phi_{ref}^{(y)}] \quad (4)$$

Applying (4), the phase reconstructions of the two orthogonal flights are now consistent to each other and the NF-FF transformation can be applied.

### C. Flow chart of the overall measurement procedure

The flow-chart in Fig. 6 highlights the fundamental steps for the characterization of a digital beamformed array by means of a non-tethered UAV performing large horizontal planar NF scans.

Regulations and UAV performances represent fundamental limitations and must be carefully taken into account in order to program a correct UAV flight trajectory. Moreover, the UAV scan size must be chosen ensuring the desired angular validity of the NF-FF transformed pattern. For this purpose, the AUT size must be known (see Section IV-C) [42]. For a complete characterization of the AUT pattern in terms of its co- and cross-polar components, two UAV rasters are needed (one raster for each field component), e.g., see Fig. 4.

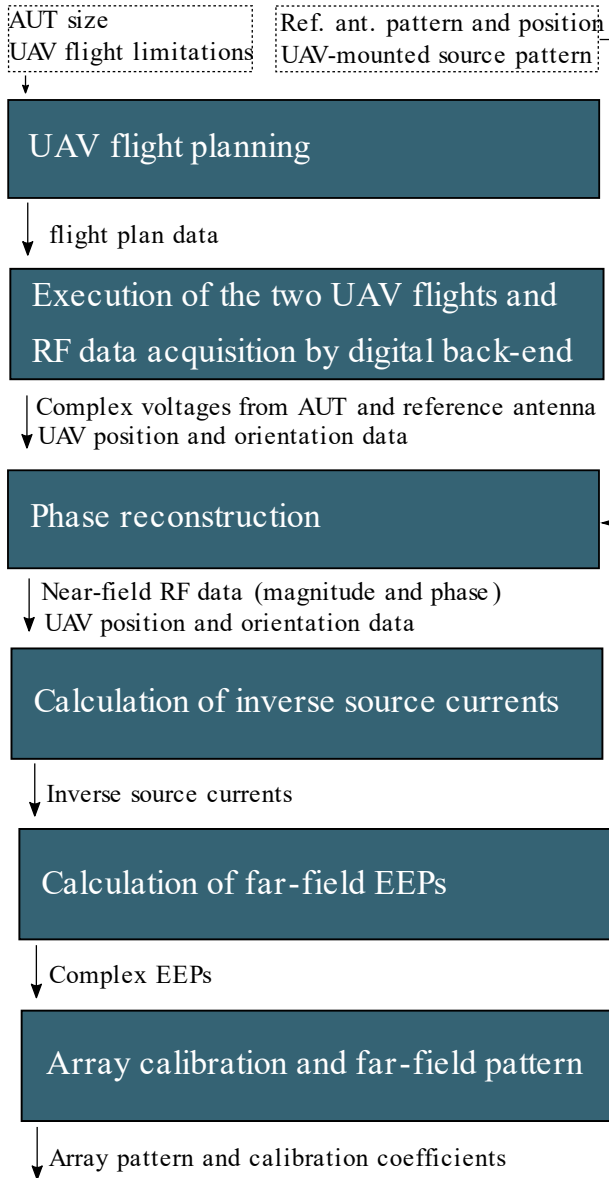


FIGURE 6. Flow chart of the proposed procedure for UAV-based NF antenna measurements.

During each flight, complex voltages are acquired at each array element by the digital beamforming back-end (see Section II). The RF data shares a consistent time reference with the UAV-mounted GNSS, i.e., they are also referenced to UTC time by means of a GNSS receiver on the ground. The correct phase information of the sampled voltages is retrieved by UAV position and orientation data, the reference antenna signal and the knowledge of their FF pattern (see Section III-B). It should be recalled that FF interaction between UAV-mounted source and reference antenna is assumed.

The NF RF data in magnitude and phase are used as input of the inverse source method to compute the equivalent currents. Then, FF EEPs are determined through radiation integrals of the computed inverse source currents.

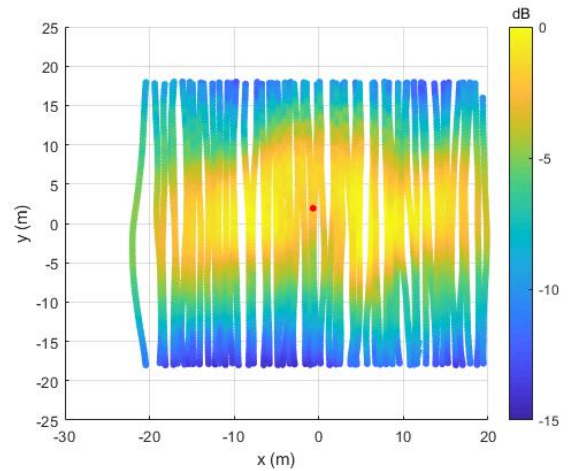


FIGURE 7. Normalized magnitude (in dB) of the measured power along the y-oriented raster for the inner element. The red dot marks the position of the inner element.

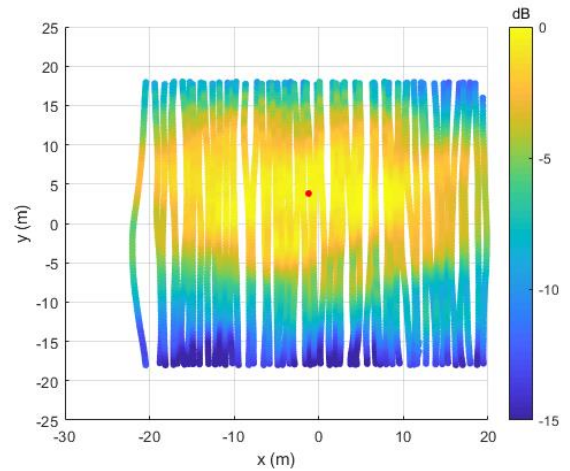


FIGURE 8. Normalized magnitude (in dB) of the measured power along the y-oriented raster for the outer element. The red dot marks the position of the outer element.

Finally, the array is calibrated equalizing the complex EEPs toward the observation direction, and the array pattern is obtained by summation.

#### IV. Results

The presented technique has been applied on the Pre AAVS1 array described in Section II to demonstrate the feasibility of the overall approach. For the sake of brevity, results for y-polarized elements are only shown. However, the same dataset (no additional flights) has been processed to determine FF patterns for the x-polarized elements with similar consistency.

Acquired NF, NF-FF inverse source transformation and FF data are presented in Section IV-A, IV-B and IV-C, respectively. The two elements labeled as “inner element” and “outer element” correspond to the two red dots in Fig. 2, 3. Finally, in Section IV-D the calibrated array beam pattern is presented.

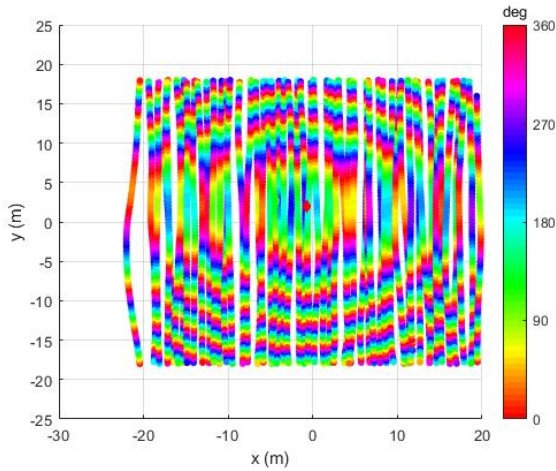


**FIGURE 9.** Reconstructed phase (deg) by (3) of the signal along the y-oriented raster for inner element. The red diamond marks the position of the inner element.

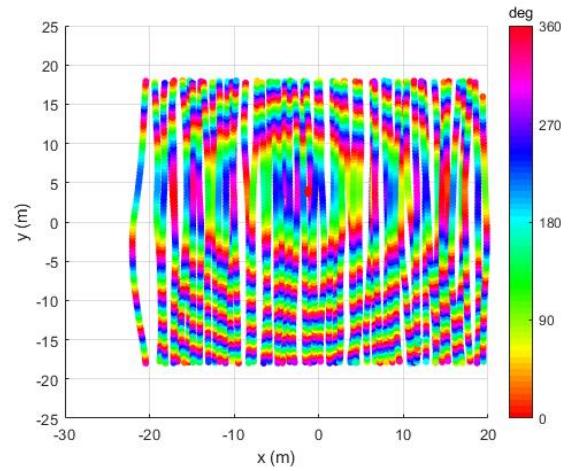


**FIGURE 11.** Reconstructed phase (deg) by (3) of the signal along the y-oriented raster for outer element. The red diamond marks the position of the outer element.

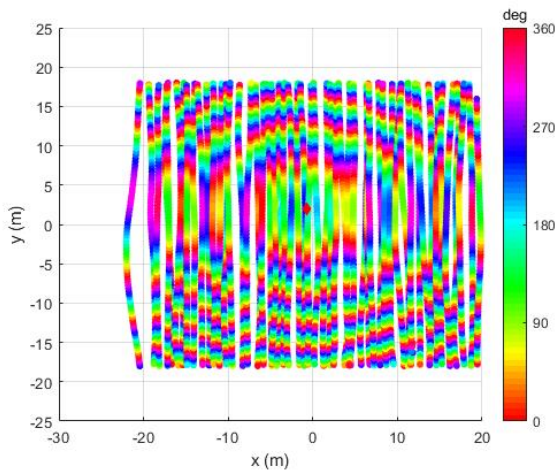


**FIGURE 10.** Simulated phase (deg) of the signal along the y-oriented raster for inner element. The red diamond marks the position of the inner element.

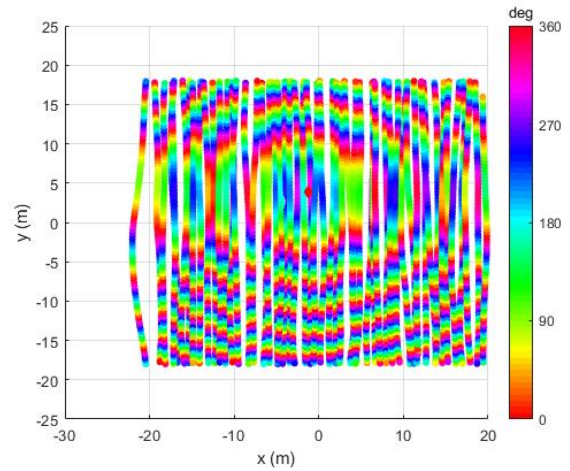


**FIGURE 12.** Simulated phase (deg) of the signal along the y-oriented raster for outer element. The red diamond marks the position of the outer element.

#### A. Measured Near-Field data

Fig. 7 - 8 show the measured NF power at 175 MHz along the UAV path (in a 2D view) received by the inner and outer elements (see red dots in Fig. 2, 3), respectively. Each measured NF pattern resembles a low-directivity radiating element whose position is highlighted with the red dot. It should be noted that, in some regions near the boundary of the scanned area, the measured power is only 5 dB lower than the maximum (see Fig. 7 - 8). As it will be stated in Section IV-C, this is not enough considering that a level of -30 dB from the maximum is generally required along the boundary of the scan plane [43]. Such limited NF scan size was dictated by the UAV flight duration. Through NF simulations (not shown here), it has been observed that the field at the boundary has a -15 dB level from its maximum when the same UAV scan in Fig. 3 - 4 is performed at half height (about 12 m). For a better fulfillment of the above-mentioned criterion, a flight at a quarter height (about 6 m) must be performed. Such an altitude is still feasible for flight safety and it will be considered for future experiments.

However, the lower flight altitude would imply higher interaction between the UAV and AUT that should be verified. On the contrary, for the considered flight (see Fig. 4) the interaction between AUT and UAV has been found to be negligible using full-wave FEKO simulations.

The phase information has been retrieved according to the procedure described in Section III-B through the dual-polarized reference antenna. The phase equalization constant  $\phi_{ref}^{(y)} - \phi_{ref}^{(x)}$  between the two orthogonal reference antenna polarizations computed through (4) is approximately  $70^\circ$ . Reconstructed phases of the inner and outer elements are shown in Fig. 9, 11. The element phase diagrams are consistent with the characteristic phase pattern of a spherical wave centered at the element position. For the sake of comparison, the simulated phases are reported in Fig. 10, 12 showing good consistency with the measured results. For the simulated phase, the electric field component along the UAV dipole direction has been computed from a complete NF simulation in FEKO. Such model included all array elements on an infinite ground-plane. The element dipoles were modeled using the thin wire approximation.

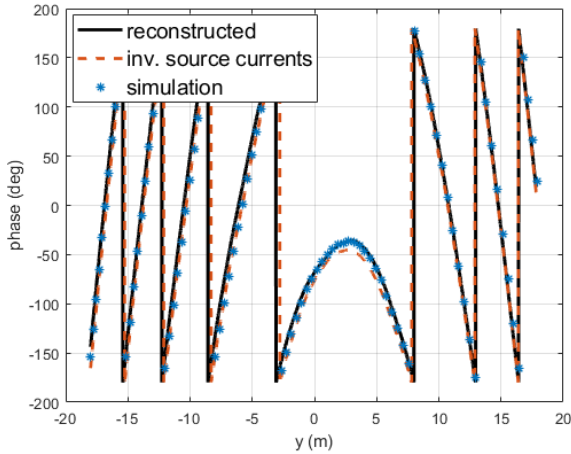


**FIGURE 13.** Reconstructed phase by (3) (black solid line) (deg), FEKO simulation (dotted blue markers) and phase of the NF field radiated by inverse source currents (dashed orange) along a quasi-linear cut at  $x=1.47$  m ( $y$ -oriented raster) for the inner element.

As a further verification, the reconstructed phase is compared to the simulated one along a quasi-rectilinear cut at  $x = 1.47$  m for the  $y$ -oriented raster. Very good agreement can be observed between the blue markers (simulation) and black solid line (reconstructed by (3)) in Fig. 13.

#### B. Inverse source

The UAV path (see Fig. 3 - 4) is not regular (neither planar nor uniformly spaced) and thus standard NF-FF transformations cannot be applied. For this reason, an inverse source approach [26] has been adopted as NF-FF transformation method. Such technique has been applied to each array element in order to compute its FF EEP. The inverse source approach is based on equivalent electric and magnetic currents placed over a virtual (non-physical) surface surrounding the AUT. These unknown currents are computed enforcing a null radiated field inside the virtual surface and a field equal to the measured one on the UAV measurement points (e.g., Fig. 7, 9 for the inner element). Through this choice, Love's currents (null field inside the virtual surface) are exploited. In this way, the computed currents are directly related to the actual electromagnetic field radiated by the AUT. The complexity of the operator that has to be inverted is increased by the addition of the null field condition. However, this choice drastically improves the condition number of the operator, resulting also in a more stable solution. It should be noted that reciprocity is exploited since the AUT is actually in receive mode. Moreover, the measurement points belong to two different raster scans (one for each flight of the UAV) and only one field component is acquired at each raster scan (see Fig. 4). The usage of equivalent currents allows enforcing different constraints at different measurement points by its very formulation (point-matching method is used to test the integral operator, i.e., it is not required that the two components are enforced at the same measurement point). This aspect has been verified applying the computational core described in [26] to a set of simulated NF data where

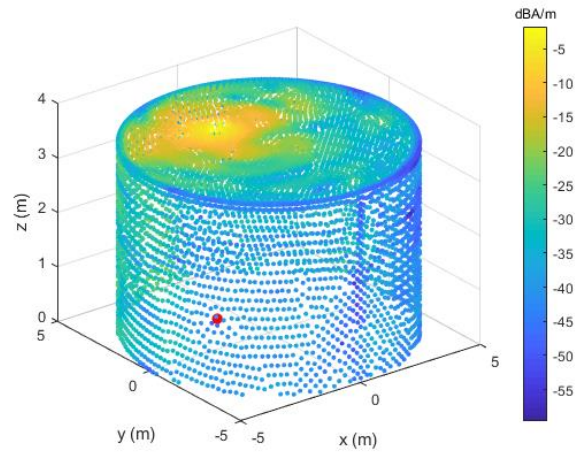


**FIGURE 14.** Magnitude of the equivalent electric current over the virtual cylindrical surface for the inner element. The red dot marks the position of the inner element.

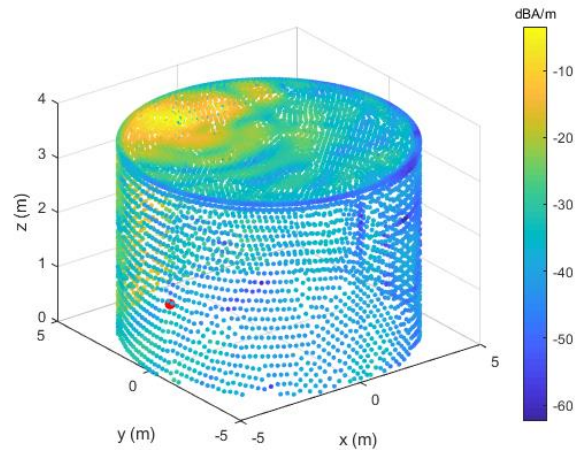


**FIGURE 15.** Magnitude of the equivalent electric current over the virtual cylindrical surface for the outer element. The red dot marks the position of the outer element.

only one field component was used for each of the two orthogonal rasters in Fig. 4. The results are not shown here because in good agreement with direct FF simulations that will be shown in Section IV-C and IV-D (maximum discrepancies of 0.3 dB and 0.5 dB for the co and cx-polar component, respectively).

A vertical cylinder of 5-m radius and 3.5-m height has been used as virtual surface (the array layout presented in Section II can be contained within a radius of 4.6 m). The presence of the ground-plane has been taken into account into the inverse-source process. The surface of the cylinder has been discretized with approximately 36.000 Rao Wilton Glisson functions [44] of order zero for a total number of 72.000 unknowns for the electric and magnetic currents. The total number of measurement points was 900.000, considering both  $x$  and  $y$ -oriented rasters. The linear system arising from the discretization has been solved in a least squares sense using an iterative method coupled with a memory saving matrix factorization and a fast matrix-vector multiplication

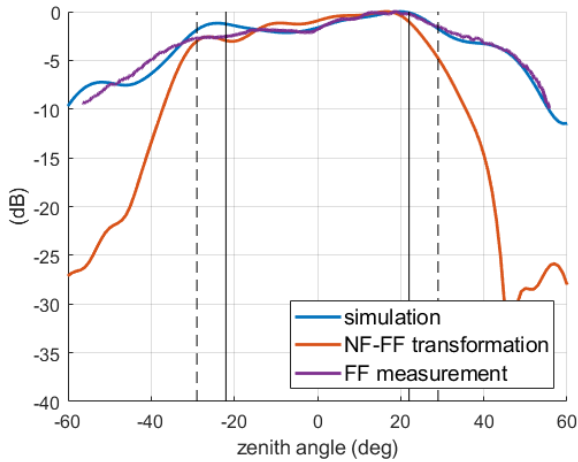


**FIGURE 16.** Normalized Embedded Element Pattern (dB) of the inner element array element. Blue, orange and purple curves represent the far field from simulation, NF-FF transformation and FF measurement, respectively. Solid and dashed black lines show the angular validity range of the NF-FF transformation (see Section IV-C).

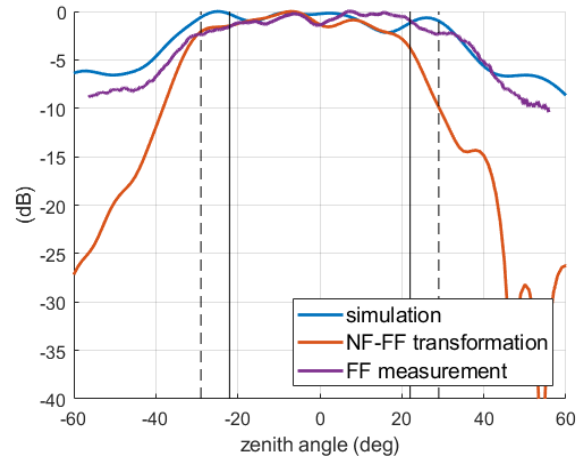


**FIGURE 18.** Normalized Embedded Element Pattern (dB) of the outer element. Blue, orange and purple curves represent the far-field from simulation, NF-FF transformation and FF measurement, respectively. Solid and dashed black lines show the angular validity range of the NF-FF transformation (see Section IV-C).

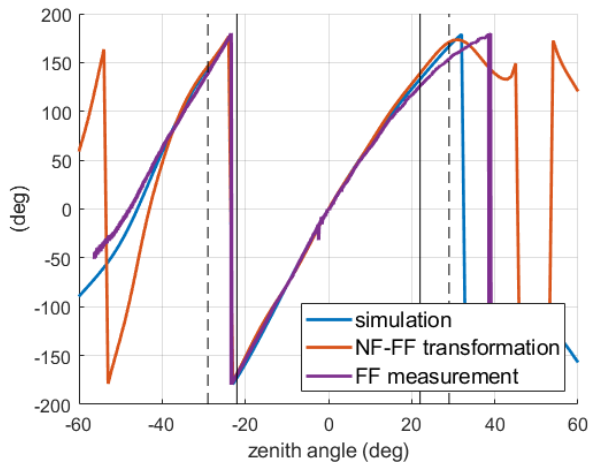


**FIGURE 17.** Embedded Element Phase Pattern (deg) of the inner element. Blue, orange and purple curves represent the far field from simulation, NF-FF transformation and FF measurement, respectively. Solid and dashed black lines show the angular validity range of the NF-FF transformation (see Section IV-C).

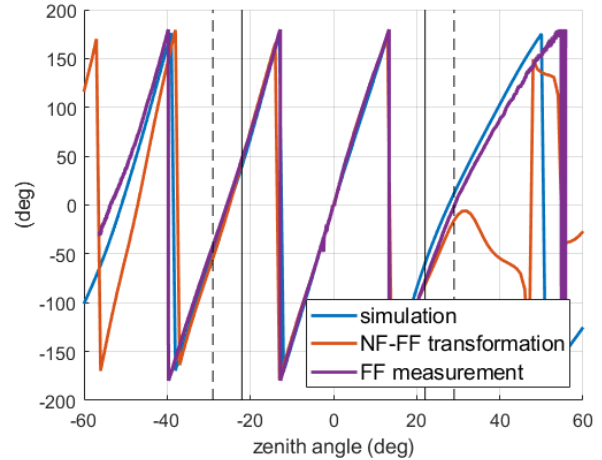


**FIGURE 19.** Embedded Element Phase Pattern (deg) of the outer element. Blue, orange and purple curves represent the far-field from simulation, NF-FF transformation and FF measurement, respectively. Solid and dashed black lines show the angular validity range of the NF-FF transformation (see Section IV-C).

[45], [46]. In this way, for each array element, the computation of the currents took approximately 16 GB of the Random Access Memory (RAM) and 32 minutes (27 for the matrix factorization and 5 minutes for the linear system solution) on a workstation with a processor Intel Xeon E5-2697 v2. Electric equivalent currents are shown in Fig. 14 - 15 for the inner and outer elements, respectively. The red dot marks the position of the considered antenna on the ground. Although currents are mainly concentrated on the upper part of the cylinder, they are non-vanishing also on its lateral part because of the finite dimension of the cylinder. Magnetic equivalent currents are not shown due to their similarity to electric ones.

As a verification example, the phase of the NF radiated from the computed equivalent currents (along a cut at  $x = 1.47$  m for the  $y$ -oriented raster) is also reported in Fig. 13 with the

orange dashed line. A good agreement can be observed between these curves, with a maximum discrepancy of approximately 10 degrees.

### C. Embedded Element Patterns (EEPs)

The radiated FF patterns at 175 MHz are computed from the equivalent currents over the cylindrical surface. NF-FF transformations exploiting larger cylinders (8 and 10 m radius) were also performed obtaining similar results to the presented case (5-m radius). Figures 16 - 19 show magnitude and phase of the transformed FF EEPs (orange solid line), co-polar component, for the inner and outer array elements highlighted in Fig. 2, 3 with red dots. For brevity, only E-plane patterns are presented in this Section.

For the sake of comparison, a FF flight was performed due to the feasible Fraunhofer distance. The UAV altitude was

approximately 100 m. A flight time of 5 minutes is required for a single FF cut. The transmitted power of 5 dBm is sufficient to achieve a good signal-to-noise ratio. Moreover, the differential GNSS position accuracy of few centimeters translates to a negligible angular error of about 0.03 degrees. Magnitude and phase of the FF EEPs have been extracted from this measurement as in [47], [48]. In particular, the reference antenna has been used also in this FF case for the computation of each EEP measured phase. This formulation exploits two independent links between UAV-mounted source and AUT and between UAV-mounted source and reference antenna. For this reason, the fulfillment of the FF condition should be satisfied considering the AUT size only (reference antenna is smaller than the AUT), i.e., without including the distance between AUT and reference antenna. The measured FF EEPs are reported with purple lines in Fig. 16 - 19. As further verification, a FF simulation has been performed in FEKO and is also reported in Fig. 16 - 19 with a blue line.

It is well known that NF planar scans suffer from some limitations. First, the transformed FF pattern of the AUT is valid only over a limited angular range. The angular bound for the validity of such transformed EEPs depends on the aperture of the AUT and both the scan size and height. Considering the array size of 9.2 m, the angular validity for the transformed FF can be estimated in the order of  $\pm 29^\circ$  [42]. On the other hand, considering the dimension of the array with its ground plane, i.e., 16 m, the maximum angle of validity reduces to  $\pm 22^\circ$ . In Fig. 16 - 19, solid and dashed vertical black lines represent the validity range of the reconstruction corresponding to  $22^\circ$  and  $29^\circ$ , respectively.

Second, as a standard requirement for NF measurement [43], the signal level at the edges of the planar scan must be 30 (or even 40) dB below the maximum. In this work, the measured power is however only 5 dB from the maximum (see Fig. 7 - 8) in some regions along the boundary. This happens because the scan size (36 - 40 m) is not large enough for the considered scan height (about 25 m). These two parameters have been selected considering flight duration and safety (to avoid collision between UAV and top of the AUT). For this reason, an even smaller angular validity (with respect to criteria discussed above) is expected in the EEPs.

It should be also mentioned that the (UAV-mounted) source dipole-like pattern has been found almost constant within the angular validity range discussed above. Therefore, probe correction issue has not been addressed in this work. Moreover, as written in Section III-A, the scan path also shows small regions where the half wavelength sampling criterion is not fully satisfied (the considered set of points in Fig. 4 has been tested using simulations, see Section IV-B). Nevertheless, results are still quite satisfactory. In Fig. 16 the agreement between NF-FF transformed and measured magnitude patterns of the inner element is reasonably good (less than 1 dB discrepancy) within the  $\pm 22^\circ$  angular region. The discrepancy is a little bit higher for the outer element. This is related to the more significant truncation effect (see Fig. 7) i.e., the element is closer to the boundary of the scan area.

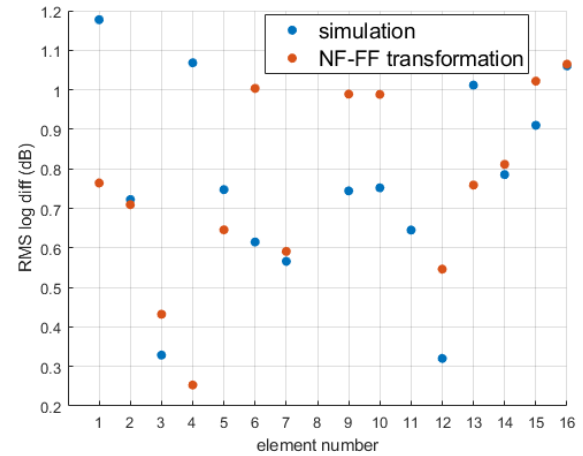


FIGURE 20. Orange (blue) line represents the Root Mean Square of the log-difference between FF measurement and NF-FF transformed (simulated) EEPs in the angular range  $22^\circ$  degrees.

As far as the phase of EEPs is concerned, as can be seen from Fig. 17, 19, the NF-FF transformations show a good agreement for both inner and outer elements.

As a figure-of-merit, the Root Mean Square (RMS) of the logarithmic difference [49] is shown in Fig. 20 for all array elements. For the sake of readability, the definition of the logarithmic difference  $LD$  is here reported

$$LD(\theta_k) = 20 \log_{10} |e_{meas}(\theta_k)| - 20 \log_{10} |e_a(\theta_k)| \quad (5)$$

where  $e_{meas}$  is the co-polar component of the measured FF EEP of the considered array element, the subscript  $a$  refers to the simulated or NF-FF transformed EEP and  $\theta_k$  is the angle of the  $k$ -th field sample. The RMS of the logarithmic difference  $LD$  (see (5)) on the  $\theta_k$  samples is reported for simulated and NF-FF transformed EEPs with blue and orange dots, respectively. The measured FF EEPs are considered as reference. The considered angular range is  $\pm 22^\circ$ . Fig. 20 suggests that the quality of the NF-FF transformed EEPs is comparable to the simulation one. Inner and outer elements are reported as element number 12 and 15, respectively (see Fig. 2). Data for element 8 are not available because that receiver channel was connected to the reference antenna. On the contrary, the error value for the NF-FF transformed EEP of element 11 is not reported because the corresponding NF measured signal exhibited lower quality due to non-optimal setting in the acquisition system. As a general remark, all measured data suffered from minor non-linearity and packet loss phenomena. Further optimization of the acquisition system setup will probably lead to smaller overall discrepancies.

#### D. Array pattern

Array calibration is a fundamental task for phased array with digital beamforming. Calibration coefficients need to be accurately determined to focus/steer the array beam in a

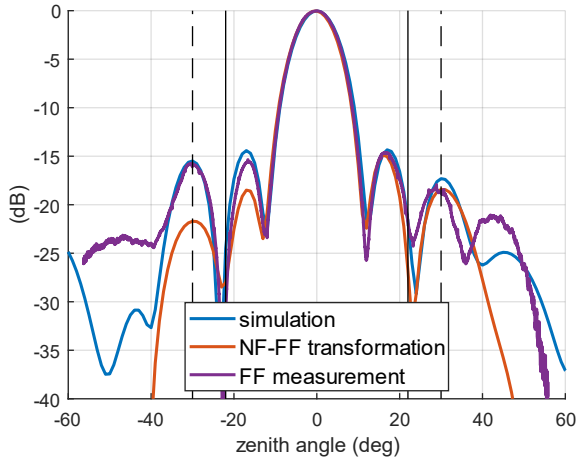


**FIGURE 21.** Normalized array pattern magnitude, E-plane cut, CO polar component. Blue, orange and purple curves represent the far-field from simulation, NF-FF transformation and FF measurement, respectively. Solid and dashed black lines show the angular validity range of the NF-FF transformation (see Section IV-C).

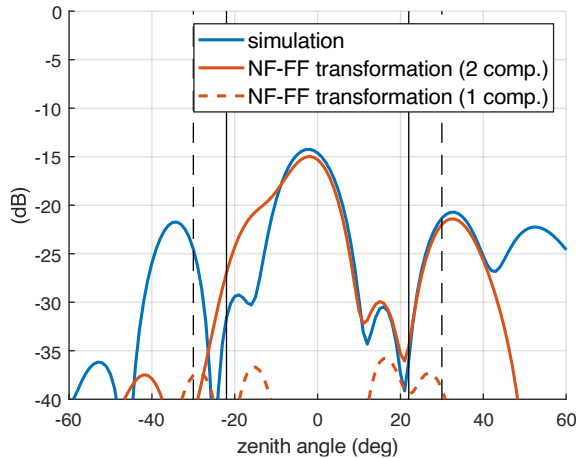


**FIGURE 22.** Normalized array pattern magnitude, E-plane cut, CX component. Blue, solid orange and dashed orange curves represent the far field from simulation and NF-FF transformation (two electric field components as input) and NF-FF transformation (only one electric field component as input), respectively. Solid and dashed black lines show the angular validity range of the NF-FF transformation (see Section IV-C).

particular direction. Such coefficients depend on both the antennas and acquisition system. The presented method represents a viable solution to determine calibration coefficients from NF measurements.

As reported in Section IV-C, all the EEPs have been obtained by NF-FF transformation from NF measurements. The calibration coefficients can be obtained by equalizing all such EEPs (in magnitude and phase) for a particular observation direction. In this way, both antenna and receiver contributions are accounted for.

The sum of all the equalized EEPs produce the full array beam. Fig. 21 shows the co-polar component of the E-plane beam pattern for the array under test pointed at zenith. The NF-FF transformation describes the main lobe and first nulls

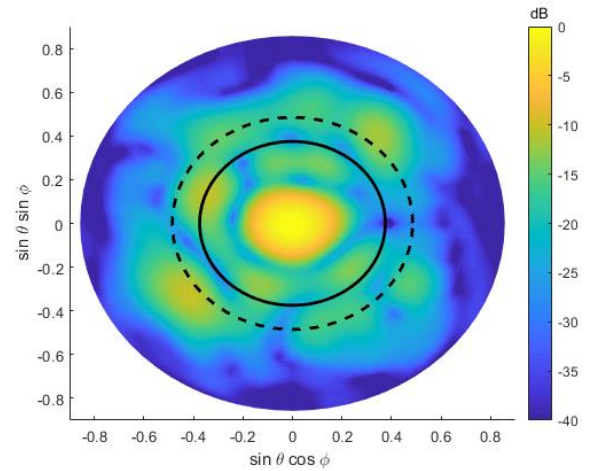


**FIGURE 23.** NF-FF transformed array beam magnitude (2D view). The black circles show the angular validity range of the NF-FF transformation (see Section IV-C).

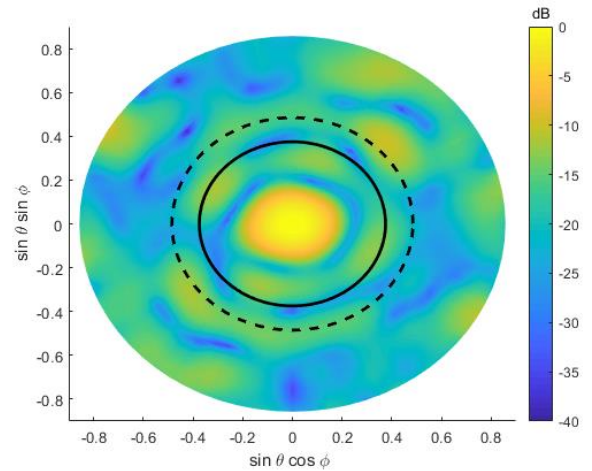


**FIGURE 24.** Simulated array beam magnitude (2D view). The black circles show the angular validity range of the NF-FF transformation (see Section IV-C).

quite well. Simulated and measured FF EEPs are reported with blue and purple lines, respectively. This validates the presented end-to-end procedure.

The cross-polar component is shown in Fig. 22. The result represented with orange solid line has been obtained with both x and y-oriented rasters in Fig. 4 whereas the orange dashed line only uses the y-oriented raster. The lack of the x-component information in the latter is clearly visible in Fig. 22. The simulated cross-polar pattern is reported with blue line (measured cross-polar FF data are not available). Even if sampling both NF components doubles the UAV flight time, this is necessary to achieve an acceptable accuracy for the cross-polar component. The good agreement between simulation (blue line) and NF-FF transformation (solid orange line) confirms the validity of the sampling approach based on two different rasters (see Fig. 4), one for each polarization.

For a complete comparison over the full azimuthal angle, Fig. 23 - 24 show the magnitude of the NF-FF transformed and simulated 2D FF array patterns pointing at zenith.

Quantities  $\theta$  and  $\phi$  correspond to the zenith and azimuth angles of the spherical coordinate system, respectively. Solid and dashed black circles correspond to  $22^\circ$  and  $29^\circ$ , respectively. As reported in Section IV-C, these angle values denote the validity of the NF-FF transformation across the zenith angular range. The agreement between the 2D patterns is quite satisfactory, i.e., main lobe size and first sidelobe locations and levels are in agreement. The 2D FF measured pattern is not available due to its prohibitive time duration (only a few FF cuts can be scanned by the UAV in a single flight [47]). For example, a complete FF pattern measurement within the  $\pm 29^\circ$  angular range with a resolution of  $1^\circ$  will require a flight duration larger than 120 minutes. It is clear that such a flight time becomes unfeasible for larger apertures where a higher Fraunhofer distance (UAV altitude) is necessary. A NF flight is instead more convenient to perform. For example, the total duration of the NF flights presented here was in the order of 30 minutes (15 minutes per electric field component). The complete FF pattern is then computed from these two NF flights through the procedure summarized in Fig. 6.

As mentioned above, in this work the NF-FF transformation has been applied separately to each array element obtaining EEPs for all the elements. Then, EEPs have been equalized (calibration) and summed together to obtain the array beam. Alternatively, if calibration coefficients are known a priori, the NF-FF transformation can be directly applied to the beamformed signal (only one NF-FF transform).

## V. CONCLUSION

A UAV equipped with a RF source has been used as an in-situ planar NF scanner covering a horizontal scan area of about  $40\text{ m} \times 40\text{ m}$ . The usage of optical fiber links from the UAV to ground has been avoided to maintain the flight flexibility and short setup time, i.e., the UAV is untethered. Furthermore, all the measurements have been performed using the acquisition system of the radio-telescope prototype instead of either a dedicated receiver or a Vector Network Analyzer (VNA).

The presented measurement setup faces the problem of the missing information of the transmitter phase. In this paper, this

## REFERENCES

- [1] A. Salari and D. Erricolo, "Unmanned Aerial Vehicles for High-Frequency Measurements: An Accurate, Fast, and Cost-Effective Technology," in *IEEE Antennas and Propagation Magazine*, doi: 10.1109/MAP.2021.3061026.
- [2] M. García-Fernández et al., "Antenna Diagnostics and Characterization Using Unmanned Aerial Vehicles," in *IEEE Access*, vol. 5, pp. 23563-23575, 2017, doi: 10.1109/ACCESS.2017.2754985.
- [3] P. Bolli et al., "From MAD to SAD: The Italian experience for the low-frequency aperture array of SKA1-LOW," in *Radio Science*, vol. 51, no. 3, pp. 160-175, March 2016, doi: 10.1002/2015RS005922.
- [4] G. Virone et al., "Strong Mutual Coupling Effects on LOFAR: Modeling and In Situ Validation," in *IEEE Transactions on Antennas and Propagation*, vol. 66, no. 5, pp. 2581-2588, May 2018, doi: 10.1109/TAP.2018.2816651.
- [5] C. Wang, B. Yuan, W. Shi and J. Mao, "Low-Profile Broadband Plasma Antenna for Naval Communications in VHF and UHF Bands," in *IEEE Transactions on Antennas and Propagation*, vol. 68, no. 6, pp. 4271-4282, June 2020, doi: 10.1109/TAP.2020.2972397.
- [6] Y. Tian, B. Wen, Z. Li, Y. Yin and W. Huang, "Analysis and Validation of an Improved Method for Measuring HF Surface Wave Radar Antenna Pattern," in *IEEE Antennas and Wireless Propagation Letters*, vol. 18, no. 4, pp. 659-663, April 2019, doi: 10.1109/LAWP.2019.2900562.
- [7] I. Farhat, D. Cutajar, K. Z. Adami, C. Sammut and J. Abela, "Characterization of 36 Meter Square Mid-Frequency Radio Astronomy Prototype Antenna Array," 2018 IEEE Conference on Antenna Measurements & Applications (CAMA), 2018, pp. 1-3, doi: 10.1109/CAMA.2018.8530622.
- [8] A. N. Cadavid, J. Aristizabal and M. D. P. Alhucema, "Antenna pattern verification for Digital TV Broadcast systems in Andean countries based on UAV's," 2018 IEEE-APS Topical Conference on

- Antennas and Propagation in Wireless Communications (APWC), 2018, pp. 858-861, doi: 10.1109/APWC.2018.8503765.
- [9] M. Heikkilä, M. Koskela, T. Kippola, M. Kocak, J. Erkkilä and J. Tervonen, "Using Unmanned Aircraft Systems for Mobile Network Verifications," 2018 IEEE 29th Annual International Symposium on Personal, Indoor and Mobile Radio Communications (PIMRC), 2018, pp. 805-811, doi: 10.1109/PIMRC.2018.8580883.
- [10] Paola Di Ninni, Pietro Bolli, Fabio Paonessa, Giuseppe Pupillo, Giuseppe Virone, Stefan J. Wijnholds, "Electromagnetic Analysis and Experimental Validation of the LOFAR Radiation Patterns", International Journal of Antennas and Propagation, vol. 2019, Article ID 9191580, 12 pages, 2019. <https://doi.org/10.1155/2019/9191580>
- [11] G. Virone et al., "Antenna Pattern Verification System Based on a Micro Unmanned Aerial Vehicle (UAV)," in IEEE Antennas and Wireless Propagation Letters, vol. 13, pp. 169-172, 2014, doi: 10.1109/LAWP.2014.2298250.
- [12] F. Paonessa et al., "UAV-based pattern measurement of the SKALA," 2015 IEEE International Symposium on Antennas and Propagation & USNC/URSI National Radio Science Meeting, 2015, pp. 1372-1373, doi: 10.1109/APS.2015.7305075.
- [13] Bolli, P., "Antenna pattern characterization of the low-frequency receptor of LOFAR by means of an UAV-mounted artificial test source", in Ground-based and Airborne Telescopes VI, 2016, vol. 9906. doi:10.1117/12.2232419.
- [14] P. Bolli, G. Pupillo, F. Paonessa, G. Virone, S. J. Wijnholds and A. M. Lingua, "Near-Field Experimental Verification of the EM Models for the LOFAR Radio Telescope," in IEEE Antennas and Wireless Propagation Letters, vol. 17, no. 4, pp. 613-616, April 2018, doi: 10.1109/LAWP.2018.2805999.
- [15] T. Fritzel et al. - Introduction into an UAV-based near-field system for in-situ and large-scale antenna measurements, IEEE Conference on Antenna Measurements & Applications (CAMA), 2016.
- [16] R. A. M. Mauermayer, J. Kornprobst and T. Fritzel, "A Low-Cost Multicopter Based Near-Field Antenna Measurement System Employing Software Defined Radio and 6-D Laser Metrology," 2019 Antenna Measurement Techniques Association Symposium (AMTA), 2019, pp. 1-5, doi: 10.23919/AMTAP.2019.8906481.
- [17] Garcia-Fernandez, M., Lopez, Y.A. and Andres, F.L.-H. (2019), Unmanned aerial system for antenna measurement and diagnosis: evaluation and testing. IET Microw. Antennas Propag., 13: 2224-2231. <https://doi.org/10.1049/iet-map.2018.6167>
- [18] R. Chandra, T. Goldstein and C. Studer, "PhasePack: A Phase Retrieval Library," 2019 13th International conference on Sampling Theory and Applications (SampTA), 2019, pp. 1-5, doi: 10.1109/SampTA45681.2019.9030878.
- [19] J. Kornprobst, A. Paulus, J. Knapp and T. F. Eibert, "Phase Retrieval for Partially Coherent Observations," in IEEE Transactions on Signal Processing, vol. 69, pp. 1394-1406, 2021, doi: 10.1109/TSP.2021.3057261.
- [20] S. Costanzo, G. Di Massa, "An integrated probe for phaseless near-field measurements", Measurement, Volume 31, Issue 2, 2002, Pages 123-129, ISSN 0263-2241, [https://doi.org/10.1016/S0263-2241\(01\)00036-7](https://doi.org/10.1016/S0263-2241(01)00036-7).
- [21] A. Paulus, J. Knapp and T. F. Eibert, "Phaseless Near-Field Far-Field Transformation Utilizing Combinations of Probe Signals," in IEEE Transactions on Antennas and Propagation, vol. 65, no. 10, pp. 5492-5502, Oct. 2017, doi: 10.1109/TAP.2017.2735463.
- [22] Costanzo, S., and Di Massa, G. (2017), Spatial domain indirect holographic technique for antenna near-field phaseless measurements, Radio Sci., 52, 432– 438, doi:10.1002/2016RS006154.
- [23] J. Laviada Martínez, A. Arboleya-Arboleya, Y. Álvarez-López, C. García-González and F. Las-Heras, "Phaseless Antenna Diagnostics Based on Off-Axis Holography With Synthetic Reference Wave," in IEEE Antennas and Wireless Propagation Letters, vol. 13, pp. 43-46, 2014, doi: 10.1109/LAWP.2013.2295735.
- [24] "IEEE Standard Test Procedures for Antennas," in ANSI/IEEE Std 149-1979, vol., no., pp.1-144, 30 Nov. 1979, doi: 10.1109/IEEESTD.1979.120310.
- [25] T. F. Eibert, E. Kilic, R. A. M. Mauermayer, O. Neitz, and G. Schnattinger, "Electromagnetic Field Transformations for Measurements and Simulations (Invited Paper)," Progress In Electromagnetics Research, vol. 151, pp. 127–150, 2015. [Online]. Available: <http://www.jpier.org/PIER/pier.php?paper=14121105>
- [26] Javier Leonardo Araque Quijano and Giuseppe Vecchi, "Field and Source Equivalence in Source Reconstruction on 3D Surfaces," Progress In Electromagnetics Research, Vol. 103, 67-100, 2010. doi:10.2528/PIER10030309
- [27] P. Bolli et al., "Test-Driven Design of an Active Dual-Polarized Log-Periodic Antenna for the Square Kilometre Array," in IEEE Open Journal of Antennas and Propagation, vol. 1, pp. 253-263, 2020, doi: 10.1109/OJAP.2020.2999109.
- [28] G. Virone et al., "The SKA Aperture Array Verification System: Measured Digitally-Beam-Formed Radiation Patterns," 2019 IEEE International Symposium on Antennas and Propagation and USNC-URSI Radio Science Meeting, 2019, pp. 395-396, doi: 10.1109/APUSNCURSINRSM.2019.8888321.
- [29] F. Paonessa et al., "SKA-Low Prototypes Deployed in Australia: Synoptic of the UAV-Based Experimental Results," URSI RADIO SCIENCE LETTERS, VOL. 2, 2020, doi: 10.46620/20-0021.
- [30] de Lera Acedo, E., Bolli, P., Paonessa, F. et al. SKA aperture array verification system: electromagnetic modeling and beam pattern measurements using a micro UAV. Exp Astron 45, 1–20 (2018). <https://doi.org/10.1007/s10686-017-9566-x>
- [31] Advancing Astrophysics With the Square Kilometre Array, SKA Organisation, Macclesfield, U.K., 2015.
- [32] de Lera Acedo, E., Razavi-Ghods, N., Troop, N. et al. SKALA, a log-periodic array antenna for the SKA-low instrument: design, simulations, tests and system considerations. Exp Astron 39, 567–594 (2015). <https://doi.org/10.1007/s10686-015-9439-0>
- [33] E. de Lera Acedo, N. Drought, B. Wakley and A. Faulkner, "Evolution of SKALA (SKALA-2), the log-periodic array antenna for the SKA-low instrument," 2015 International Conference on Electromagnetics in Advanced Applications (ICEAA), 2015, pp. 839-843, doi: 10.1109/ICEAA.2015.7297231.
- [34] G. Naldi, et al., "The Digital Signal Processing Platform for the Low Frequency Aperture Array: Preliminary Results on the Data Acquisition Unit," 2017, Journal of Astronomical Instrumentation, 06, 1641014
- [35] A. Magro et al., "A software infrastructure for firmware-software interaction: The case of TPMs," 2017 International Conference on Signals and Systems (ICSigSys), 2017, pp. 190-196, doi: 10.1109/ICSIGSYS.2017.7967039.
- [36] A. Magro, K. Bugeja, R. Chiello and A. DeMarco, "A High-Performance, Flexible Data Acquisition Library for Radio Instruments," 2019 IEEE-APS Topical Conference on Antennas and Propagation in Wireless Communications (APWC), 2019, pp. 069-074, doi: 10.1109/APWC.2019.8870490.
- [37] Kerns, D. M., "Plane-wave scattering-matrix theory of antennas and antenna-antenna interactions: Formulation and applications," Journal of Research of the National Bureau of Standards, vol. 80B, no. 1, pp. 5-51, 1976.
- [38] F. D'Agostino, F. Ferrara, C. Gennarelli, R. Guerriero, S. McBride and M. Migliozzi, "Fast and Accurate Antenna Pattern Evaluation From Near-Field Data Acquired via Planar Spiral Scanning," in IEEE Transactions on Antennas and Propagation, vol. 64, no. 8, pp. 3450-3458, Aug. 2016, doi: 10.1109/TAP.2016.2576483.
- [39] F. D'Agostino, F. Ferrara, C. Gennarelli, R. Guerriero and M. Migliozzi, "An SVD-Based Approach to Reconstruct the Planar Wide-Mesh Scanning NF Data From Inaccurately Probe-Positioned Samples," in IEEE Antennas and Wireless Propagation Letters, vol. 17, no. 4, pp. 641-644, April 2018, doi: 10.1109/LAWP.2018.2808424.
- [40] L. Ciorba et al., "Near-Field Phase Reconstruction for UAV-based Antenna Measurements," 2019 13th European Conference on Antennas and Propagation (EuCAP), 2019, pp. 1-4
- [41] Constantine A. Balanis, "Fundamental Parameters and Figures-of-Merit of Antennas," in Antenna Theory: Analysis and Design, Wiley, 2016, pp.25-126.
- [42] A. C. Newell, "Error analysis techniques for planar near-field measurements," in IEEE Transactions on Antennas and Propagation, vol. 36, no. 6, pp. 754-768, June 1988, doi: 10.1109/8.1177.
- [43] "IEEE Recommended Practice for Near-Field Antenna Measurements," in IEEE Std 1720-2012, vol., no., pp.1-102, 5 Dec. 2012, doi: 10.1109/IEEESTD.2012.6375745.
- [44] S. Rao, D. Wilton and A. Glisson, "Electromagnetic scattering by surfaces of arbitrary shape," in IEEE Transactions on Antennas and

- Propagation, vol. 30, no. 3, pp. 409-418, May 1982, doi: 10.1109/TAP.1982.1142818.
- [45] L. Scialacqua, F. Mioc, L. J. Foged, G. Giordanengo, M. Righero and G. Vecchi, "Diagnostics on electrically large structures by a nested skeletonization scheme enhancement of the equivalent current technique," 2020 14th European Conference on Antennas and Propagation (EuCAP), Copenhagen, Denmark, 2020, pp. 1-4. doi: 10.23919/EuCAP48036.2020.9135891
- [46] L. Scialacqua, F. Scattone, A. Giacomini, L. J. Foged and F. Mioc, "Advanced Diagnostics on a Large Array by the Equivalent Current Technique," 2021 Antenna Measurement Techniques Association Symposium (AMTA), 2021, pp. 1-5, doi: 10.23919/AMTA52830.2021.9620592.
- [47] Giuseppe Virone, Fabio Paonessa, Lorenzo Ciorba, Stefania Matteoli, Pietro Bolli, Stefan J. Wijnholds, Giuseppe Addamo, "Measurement of the LOFAR-HBA beam patterns using an unmanned aerial vehicle in the near field," J. Astron. Telesc. Instrum. Syst. 8(1), 011005 (2022), doi: 10.1117/1.JATIS.8.1.011005.
- [48] G. Virone et al., "Antenna pattern measurements with a flying far-field source (Hexacopter)," 2014 IEEE Conference on Antenna Measurements & Applications (CAMA), 2014, pp. 1-2, doi: 10.1109/CAMA.2014.7003370.
- [49] S. Pivnenko et al., "Comparison of Antenna Measurement Facilities With the DTU-ESA 12 GHz Validation Standard Antenna Within the EU Antenna Centre of Excellence," in IEEE Transactions on Antennas and Propagation, vol. 57, no. 7, pp. 1863-1878, July 2009, doi: 10.1109/TAP.2009.2021934.



**LORENZO CIORBA** received the master's degree (110/110) in mathematical engineering from Politecnico di Torino, Italy, in March 2018, with the thesis "Hybrid Antenna Measurement and Simulations" with Prof. G. Vecchi as a supervisor. In June 2018, he joined the Applied Electromagnetics and Electronic Devices Group of the Institute of Electronics, Computer and

Telecommunication Engineering (IEIIT), Italian National Research Council (CNR), as a Research Fellow. From November 2018, he has been a Ph.D. student in electrical, electronics and Communications Engineering at Politecnico di Torino. His scientific interests regard computational electromagnetics and characterization of antennas, in particular UAV-based near-field antenna measurements.



**GIUSEPPE VIRONE** (M'05–SM'21) was born in Turin, Italy, in 1977. He received the degree in Electronic Engineering (summa cum laude, November 2001) and the PHD in Electronics and Communication Engineering (2006) at the Politecnico di Torino, Turin, Italy. He is currently a senior researcher at the Istituto di Elettronica e di Ingegneria Informatica e delle Telecomunicazioni (IEIIT), Italian National Research Council (CNR). He joined IEIIT as a research assistant in

2002. He coordinated more than 15 scientific projects funded by both the industry and other scientific research organizations and joined more than 30 research projects as a collaborator. He authored 43 journal papers, 134 conference papers and 3 European patents. His activities concern the design, numerical analysis and characterization of microwave and millimeter passive components for feed systems, antenna arrays, frequency selective surfaces, compensated dielectric radomes and industrial sensing applications.



**Fabio Paonessa** (M'18) was born in Turin, Italy, in 1985. He received the BS and the MS degrees in biomedical engineering and the PhD degree in electronics engineering from Polytechnic of Turin, in 2008, 2010, and 2017, respectively. From 2011 to 2012, he was a Research Assistant with the Department of Electronics, Polytechnic of Turin. His activities concerned the design of electronic systems to generate high-intensity focused

ultrasounds for sonodynamic therapy. In 2013, he joined the Applied Electromagnetics Group of CNR-IEIIT, where he became Researcher in 2018. His current activities include UAV-based characterization of antenna arrays and radar systems, UAV applications in wireless sensor networks, and design of microwave waveguide passive components.

**ELOY DE LERA ACEDO** ('10 PhD) leads the radio astronomy group at Cavendish Astrophysics, University of Cambridge. He was recently awarded a STFC Ernest Rutherford Fellowship to work in studies of the infant universe. His research interests include radio cosmology, electromagnetic theory and modelling, electromagnetic metrology and antenna design.



**STEFANIA MATTEOLI** (S'06, M'11, SM'17) received her B.S. and M.S. (cum laude) degrees in Telecommunications Engineering and the Ph.D. in "Remote Sensing" from University of Pisa, Italy, in 2003, 2006, and 2010 respectively.

She is currently a permanent researcher at the National Research Council of Italy within the Institute of Electronics, Information Engineering and Telecommunications. From January 2010 to December 2016, she was first a post-doctoral fellow and then

a temporary researcher with the Department of Information Engineering, University of Pisa, Italy. From May 2008 to October 2008, she was a visiting student at the Chester F. Carlson Center for Imaging Science, Rochester Institute of Technology, Rochester, New York. Her main research interests include signal and image processing applied to various fields such as hyperspectral remote sensing, submarine remote sensing with fluorescence LIDAR, food safety and agriculture, and UAV-based antenna array calibration. Dr. Matteoli is Associate Editor of the IEEE GEOSCIENCE AND REMOTE SENSING LETTERS and of the SPIE *Journal of Applied Remote Sensing*. She has served as reviewer for many journals in the field of remote sensing and signal processing. In 2014 she was a recipient of the "SPIE Remote Sensing Europe Best Student Paper Award" within the 'Remote Sensing of the Ocean, Sea Ice, Coastal Waters, and Large Water Regions' conference, for the paper entitled "Design and validation of object recognition methodologies for underwater fluorescence lidar applications."



**PIETRO BOLLI** received his Laurea degree in electronic engineering and his PhD in computer science and telecommunications engineering from the University of Florence, Florence, Italy, in 1999 and 2003, respectively. In 2002, he started his professional career as a microwave engineer at the Italian National Institute for Astrophysics (INAF) conducting research in the field of technology applied to radio astronomy. He is currently senior technologist at the INAF Arcetri Astrophysical Observatory. He is a co-author of about 140 scientific publications, which have appeared in international referred journals and conferences.



**OSCAR A. PEVERINI** was born in Lisbon, Portugal, in April 1972. He received the Laurea degree in Telecommunication Engineering (summa cum laudae) and the Ph. D. degree in Electronic Engineering at the Politecnico di Torino, Italy, in 1997 and 2001 respectively. During his doctoral studies, he was a visiting researcher at the University of Paderborn, Germany, where he was involved in the design of acousto-optical devices. In 2001 he was a research fellow at the Physics Department of the Politecnico di Torino and at the

CNR-IRITI institute. In December 2001, he joined the CNR-IEIIT institute as a permanent-position researcher. Since 2021, he is a Director of Research in the same institute. Since 2009 he is the responsible coordinator of the CNR-IEIIT Applied Electromagnetics and Electronic Devices research unit. He has been the technical manager for several scientific programmes and industrial research contracts aimed at the development of microwave and millimeter-wave devices for space-born applications. He has been serving as a reviewer for several journals and conferences in the microwave area. He has authored and co-authored over 50 journal papers, 100 conference papers, and he is co-inventor of 3 European patents. He serves as chairman of the ICT evaluation board for the Sustainable Growth Fund Programme of the Italian Ministry Economic Development.



**GIUSEPPE ADDAMO** was born in Messina, Italy, in 1979. He received the Laurea degree (summa cum laude) in electronic engineering and Ph.D. degree in electronic and communication engineering from the Politecnico di Torino, Turin, Italy, in 2003 and 2007, respectively. In January 2007, he joined the Istituto di Elettronica e di Ingegneria dell'Informazione e delle Telecomunicazioni (IEIIT), Consiglio Nazionale delle Ricerche (CNR), Turin, Italy, as a Research Fellow, and in 2012, became a Researcher. He holds practical classes in courses on electromagnetic field theory and mathematical analysis at the Politecnico di Torino. His research interests are in the areas of microwave leaky antennas, dielectric radomes, high-power feed systems (e.g., orthomode transducers (OMTs), microwave filters), corrugated horns, frequency-selective surfaces, and large dielectric radomes.

